Scanning photoelectron spectromicroscopy: from static to operando studies of functional materials

M. Amati[1], Toma Susi[2], P. Jovičević-Klug[3], M. Jovičević-Klug[3], Tomasz Kosmala[4,5], Gaetano Granozzi[4], Stefano Agnoli[4], Pengfei Yang[6], Yanfeng Zhang[6], Mattia Scardamaglia[7] and L. Gregoratti[1]

[1] Elettra – Sincrotrone Trieste ScpA, SS14-Km163.5 in Area Science Park, Trieste, Italy

[2] University of Vienna, Faculty of Physics, Boltzmanngasse 5, 1090 Vienna, Austria

[3] Max-Planck-Institute for Iron Research, Max-Planck-Str. 1, 40237 Düsseldorf, Germany

[4] Department of Chemical Sciences, University of Padova, Padova 35131, Italy

[5] Institute of Experimental Physics, University of Wrocław, Wrocław 50-204, Poland

[6] Peking University, Yiheyuan Rd, Haidian District, Beijing, Cina, 100871

[7] Max IV Laboratory - Lund University, Fotongatan 2, 22484 Lund, Sweden

Abstract

The scanning photoelectron microscope (SPEM), developed more than 30 years ago, has undergone numerous technical developments, providing an incredibly vast kind of feasible sample environments, which span from the traditional high spatial resolution core level based chemical analysis to *in-situ* and *operando* complex experiments, including also electrochemical setups and multi-biased electronic devices at various temperatures. Another important step ahead is overcoming the so-called pressure gap for *operando* studies, recently extended to near ambient values by building special environmental cells. Using recent results of conventional and unconventional experiments, obtained with SPEM at the ESCA Microscopy beamline at Elettra-Sincrotrone Trieste the present review demonstrates the current potential of this type of photoelectron spectromicroscopy to explore the interfacial properties of functional materials with high spatial resolution.

1.   Introduction

Scanning photoelectron microscopes (SPEMs) were originally designed to perform standard ultra-high vacuum (UHV) characterization of samples adding submicrometer spatial resolution to the X-ray photoelectron spectroscopy [1]. It should be pointed out that at the synchrotron facilities, along with SPEMs, the full field imaging X-ray photoelectron emission microscopes (PEEM or XPEEM) have also been implemented, where magnified image of the emitted photoelectrons from the probed area is obtained using electrostatic and/or magnetic lenses to convert the electron signal into visible light [2]. The scanning (SPEM) and full-field (PEEM) approaches are complementary, XPEEMs are more suitable for fast imaging with high spatial

resolution, combined with XPS and/or X-ray absorption spectroscopy (XAS), and SPEMs more prone to using imaging and high energy resolution XPS for investigating samples with complex morphologies [3]. Now the major fields of research spanning over heterogeneous catalysis to the more recent ultrathin materials and composites media are the playground of these microscopes, in particular when the sample surface has a marked topography [4–7]. Over the decades scientists and engineers have continuously enriched the SPEM capabilities, aiming to overcome the limited *in-situ* or *operando* capabilities due to the technical complexities introduced by the presence of the zone plate focusing optics, which strongly constraints the space and the environment around the samples.

In current times, the existing SPEMs are hosted by the 3rd generation synchrotron facilities. The ones operating in the soft X-ray range perform XPS imaging and microspectrosopy, the other operating in the VUV range are using angular resolved photoemission spectroscopy (ARPES) and a few combines both approaches, introducing additional entanglements in the microscope design [8–12]. Depending on the desired performance, SPEMs can choose different photon focusing optics: diffractive lenses - zone plates (ZP) or mirrors such as the Kirkpatrick–Baez (KB) or Schwartzschild configuration or reflective optics such as x-ray collimating capillaries.

The SPEM, hosted at the ESCA Microscopy beamline at the Elettra synchrotron was commissioned in 1994 and has served the users community since 1995 [13]. It works in the soft X-ray energy range and uses a zone plate (ZP) focusing system. The microscope has undergone many technical upgrades, which have expanded its capabilities also for *in-situ* and *operando* sample analysis. The possibility of sample annealing and cooling during *operando* measurements is implemented using different tools and approaches fitting best to each type of experiment, as well as the capability to charge different areas of the same sample with dedicated contacts, as happens in electrochemical reactions. Another recent upgrade has also extended the allowable pressure regime of operation to the near ambient and ambient ranges.

This manuscript reports the present performance of the SPEM at Elettra, using selected results from standard and unconventional experiments with various users, demonstrating the SPEM vitality and uniqueness for different important research areas of material science.

2.   Layout and technical specification of the SPEM of the ESCA Microscopy beamline at Elettra

The X-rays at the ESCA microscopy beamline at Elettra [14] are provided by a 4.6 m long Linearly Polarized Undulator and the photon energy (400–1200 eV range) is set by a spherical grating monochromator. The SPEM X-ray focusing set-up consists of a focusing ZP lens and an order sorting aperture (OSA) to eliminate the contamination from the unwanted diffraction orders. Depending on the need for photon energy and spatial resolution, ZPs with different dimensions, within the range of 200-250 µm diameter with 50–100 nm outermost ring width are used. The focusing system can de-magnify the photon beam down to a spot of 130–180 nm diameter providing a focal length in the 5–15 mm range, with both the spot dimension and focal length being function of the photon energy.
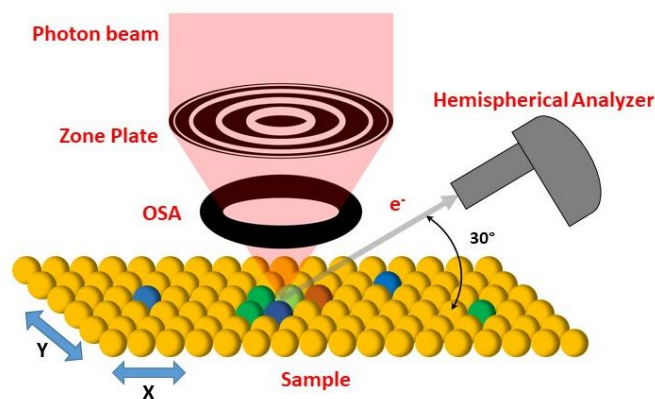
Fig. 1. Layout of the SPEM at the ESCA Microscopy beamline at Elettra. An optics system composed by a zone plate and an OSA focuses the incoming X-ray beam normally to the sample surface. Emitted photoelectrons are collected at a 30°grazing angle by hemispherical electron analyzer. Samples can be XY scanned for imaging and nano-positioning.

As sketched in Fig. 1, samples are positioned in the focal point of the optics, working in normal X-ray incidence. Samples can be raster scanned, in the plane orthogonal to the beam, by sets of stepper and piezoelectric motors. Due to the geometric restrictions imposed by the short focal length, in order to optimally detect emitted photoelectrons the Hemispherical Electron Analyzer (HEA) with maximum acceptance angle is ±10° is at a take-off-angle of 30° with respect to the sample surface. This configuration strongly enhances the surface sensitivity of the instrument; detected photoelectrons around 100 eV kinetic energy come typically from the topmost two monolayers of the surface. The HEA is equipped with a delay line electron detector that is binned to 48-channels [15].

The SPEM can operate in two modes: (1) imaging spectro-microscopy and (2) micro-spot XPS. The imaging mode maps the lateral distribution of elements or chemical states by collecting photoelectrons within a selected kinetic energy window while scanning the specimen with respect to the microprobe. The micro-spot spectroscopy mode is identical to conventional XPS, but the probed areas are selected submicron spots from the maps of the the sample. The best overall energy resolution at room temperature at 500 eV photon energy is below 200 meV.

3.   Results and discussion

3.1   *Intrinsic core level photoemission of suspended monolayer graphene*

Graphene is an interesting model system for photoemission physics, as due to the excitation of low-energy electron-hole pairs that screen the core hole, its C 1*s* signal is significantly asymmetric towards higher core-level binding energies [16]. Further, although the localised core electrons do not participate in chemical bonding, synchrotron XPS has revealed that the core level does show some dispersion [17]. However, although the C 1*s* core-level BE of bulk graphite has been accurately measured at 284.42 eV [18], due to the extreme sensitivity of

two-dimensional graphene to its environment, it was not clear what the intrinsic value of its C 1s level is. Graphene is typically grown on metallic substrates, where the measured monolayer BEs vary from as low as 283.97 eV [19] to as high as 284.7 eV [20], while a measurement of epitaxial monolayer graphene on SiC suggested an upshift of 0.4 eV compared to four graphene layers [21]. Further, ubiquitous surface contamination, localised multilayer grains, defects such as grain boundaries, and even chemisorbed species have complicated the measurement of an intrinsic value.

Recently we were able to combine SPEM with aberration-corrected scanning transmission electron microscopy (STEM) and Raman spectroscopy performed on the same identified sample areas on a TEM support grid to address this issue [22]. Samples were shipped in a protective atmosphere between Elettra in Trieste, where photoemission was measured, and the STEM laboratory in Vienna, where the samples were cleaned, and characterised both before and after the SPEM measurement. By confirming the monolayer nature of the measured areas with Raman and STEM, and characterising the spatial distribution of the surface contamination and any defects present (see Fig. 2), it was possible to determine that the intrinsic C 1s BE of the graphene monolayer is 284.70±0.05 eV, with a full width at half maximum of 0.44 eV and a Doniach-Šunjić asymmetry parameter of 0.095. The BE was thus found to be 0.28 eV higher than that of graphite [22].
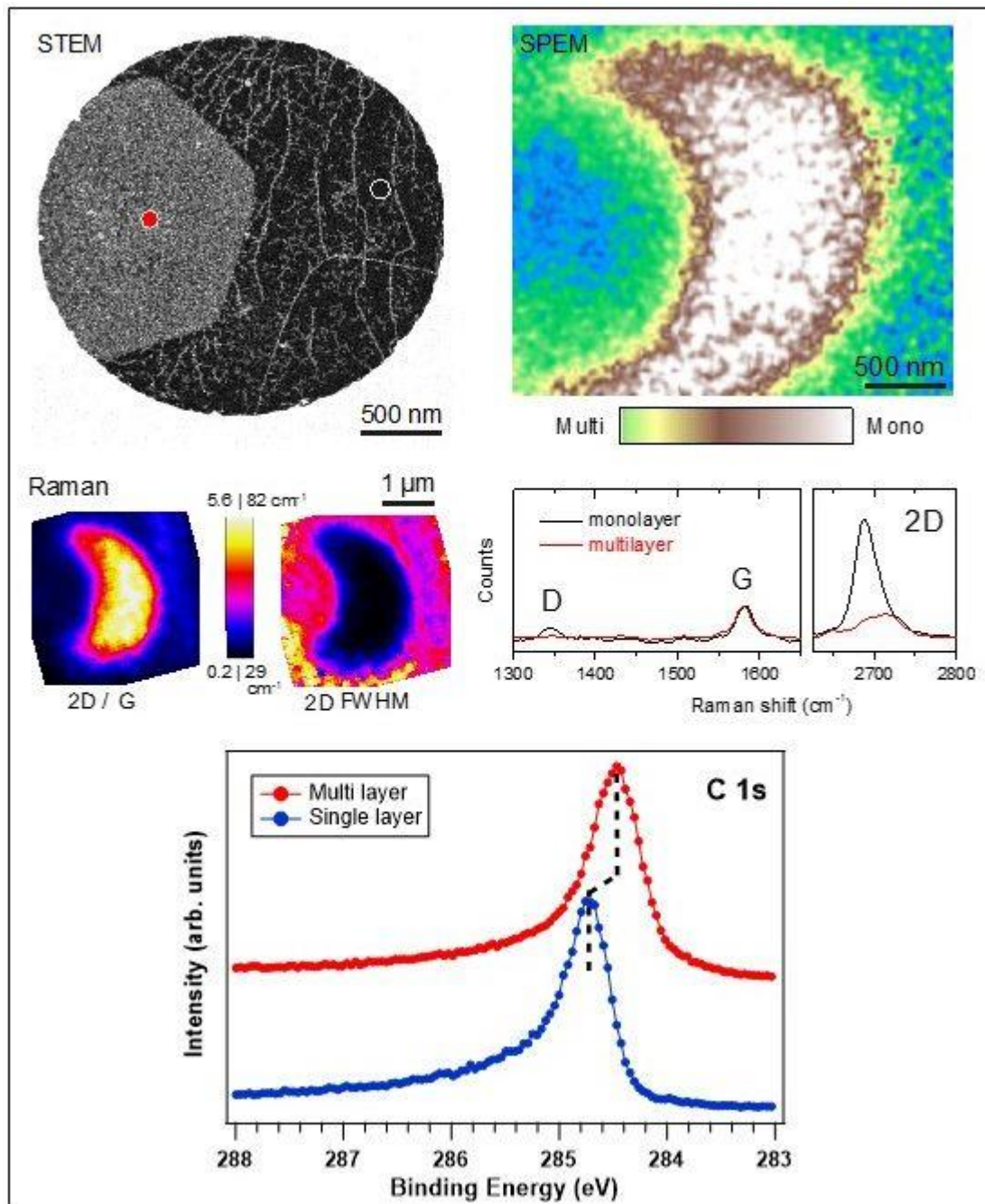
Fig. 2: Combined scanning transmission electron microscopy (STEM), scanning photoelectron microscopy (SPEM) and Raman spectroscopy measurement of the same area of suspended monolayer graphene with an overlying multilayer grain. Both STEM and Raman measurements confirm that the suspended area is mainly a monolayer, with the linear speckled contrast corresponding to contamination-decorated wrinkles and a grain boundary on the bottom right-hand side (for further characterization, see Ref. [22]). The coloured circles overlaid on the STEM image correspond to the size of the SPEM X-ray spot, allowing the photoemission signal from a clean part of the monolayer to be accurately pinpointed (the colouring of the SPEM image corresponds to the ratio of signal corresponding to monolayer and multilayer graphene).C 1s core-levels signals acquired on the mono- and multilayer graphene. [Adapted figure with permission from Toma Susi et al. PHYSICAL REVIEW MATERIALS 2, 074005 (2018). Copyright (2018) by the American Physical Society].

The upper images in Fig. 1 show a STEM (left) and SPEM C 1s (right) maps of the same suspended graphene area. Electron microscopy evidences a well-defined multilayer region on the left surrounded by monolayer graphene where linear wrinkles and smaller defected/thicker zones are present. Despite the different spatial resolution, the SPEM map as well as the Raman images showing the 2D/G components ratio and the 2D full width half maximum distribution align perfectly to confirm this scenario. The Raman spectra have been acquired in the areas indicated in the STEM map.

We further determined [22] that bilayer and four-layer values lie respectively at 284.54 and 284.47 eV, revealing a linear trend as a function of layer number as was expected based on epitaxial graphene [21]. However, since our samples were suspended, we are confident that these shifts are due to differences in the intrinsic screening of the core hole, further confirmed by concurrently measured valence-band photoemission that showed no shift of the Dirac point within our energy resolution. Finally, while we found that both contamination and grain boundaries broaden the C 1s signal, explainable by the convolution of signals from the carbonaceous contaminants and possibly non-sp^2 carbon of the lattice itself with the graphene spectrum, these do not significantly affect the peak position [22].

These measurements demonstrate the absolute necessity of the high spatial and energy resolution afforded by synchrotron-based SPEM to accurately characterize low-dimensional materials, as well as the crucial contribution to understanding that complementary microscopic and spectroscopic tools can offer. Although such measurements are far from trivial, using TEM support grids with positional markers made it relatively easy to locate the exact same sample areas using all three characterization techniques.

3.2 Elucidation of the mechanism of deep cryogenic treatment of high-alloyed ferrous alloy by in-situ low-temperature scanning photoelectron microscopy investigation

The investigation of the effect of deep cryogenic treatment (DCT) on a high-alloyed ferrous alloy (HAFA) and its effectiveness on carbide evolution and chemical shifts of alloying elements was performed with both ex-situ and in-situ cryogenic SPEM to probe chemical changes induced by DCT. DCT is a type of treatment by exposing materials to temperatures below 123 K (usually of liquid nitrogen or liquid helium) [23], inducing changes in material's microstructure and properties (surface and mechanical properties, magnetic characteristics, corrosive and wear resistance etc.) [23–25]. Various studies [24,26–30] have associated DCT with increased nucleation and precipitation of carbides, matrix transformation (from retained austenite to martensite), more homogeneous microstructure and modified internal stresses [31,32]. However, many unknowns remain regarding the mechanism(s) of DCT, particularly in relation to surface modification and surface chemistry, which is predicted to be the main reason for the improved corrosion and wear resistance of treated materials [24,25,33,34].

Microstructural analysis by scanning electron microscopy (SEM), energy dispersive X-ray spectroscopy (EDX), atomic probe tomography (APT) and small angle neutron scattering (SANS) identified the following main phases in the samples [24,35]: martensite, M_7C_3, and $M_{23}C_6$ carbides. M_7C_3 carbides are enriched with Mo and $M_{23}C_6$ have lower Cr, V and Mo content, but display a Cr-rich shell [24,35]. SANS confirmed a large number of $M_{23}C_6$ carbides with the size range of 1-4 nm [24,35].

Ex-situ SPEM was used to study the evolution and behaviour of selected alloying elements during the nucleation of carbides formed during the different heat treatment routes: conventional heat treatment (CHT) with samples austenitized at T_a = 1323 K for 2 min, quenched in nitrogen gas and triple tempered at T_t = 873 K for 2 h and DCT samples austenitized at T_a = 1323 K for 2 min, quenched in nitrogen gas, exposed to liquid nitrogen temperatures at T=77 K for 24 h and finally tempered at T_t = 873 K for 2 h [24]. Overall, the SPEM maps (Fig. 3(a) and (b)) show the clear separation of MC and M_6C carbides by their V and W contents [24]. Furthermore, microspectroscopy C 1s analysis (Fig. 3(c) and (d)) of carbides present in CHT or DCT show a difference in the C binding state, C 1s spectrum is shifted towards lower BE (~283 eV) in MC type of carbides compared to M_6C (~284 eV BE). This is correlated with the highly C-enriched state of MC carbides [24]. In M_6C carbides, C is located within the octahedral interstitial sites, less tightly bonded to metal atoms due to its high ligancy [36]. As a result, the C 1s chemical shift is similar to the shift within the matrix [24]. Additionally, the core-shell structure of MC carbides is confirmed by the double peak character of C 1s. SPEM also confirms the different evolution of $M_{23}C_6$ carbide with CHT and DCT, indicating higher alloying and larger size in the CHT sample compared to the DCT one (Fig. 3(a) and (b)).

Core level spectra analysis confirms that $M_{23}C_6$ carbides evolve towards the M_6C composition with the slight presence of Mo, W and V [24]. The comparison of both heat treatments (CHT and DCT) revealed the higher V content of CHT carbides than of DCT ones. In addition, DCT induces higher Mo content in $M_{23}C_6$ (Fig. 3(c) and (d)), whereas CHT $M_{23}C_6$ carbides do not show this trend, but have higher Cr and C contents [24].

In-situ SPEM at cryogenic temperatures revealed the underlying mechanism of C redistribution and chemical state changes of the alloying elements [24]. The results indicate that C is redistributed towards the vicinity of pre-existing carbides and defects, which does not influence the binding states of C during DCT cooling, but after the material is heated up. Moreover, a change in the binding state of Mo is recorded, showing a slight shift of 0.1-0.2 eV during DCT [24]. The observed phenomenon is particularly visible around smaller prior M_6C carbides. With a line scan of the Mo spectra over selected carbides and the surrounding matrix
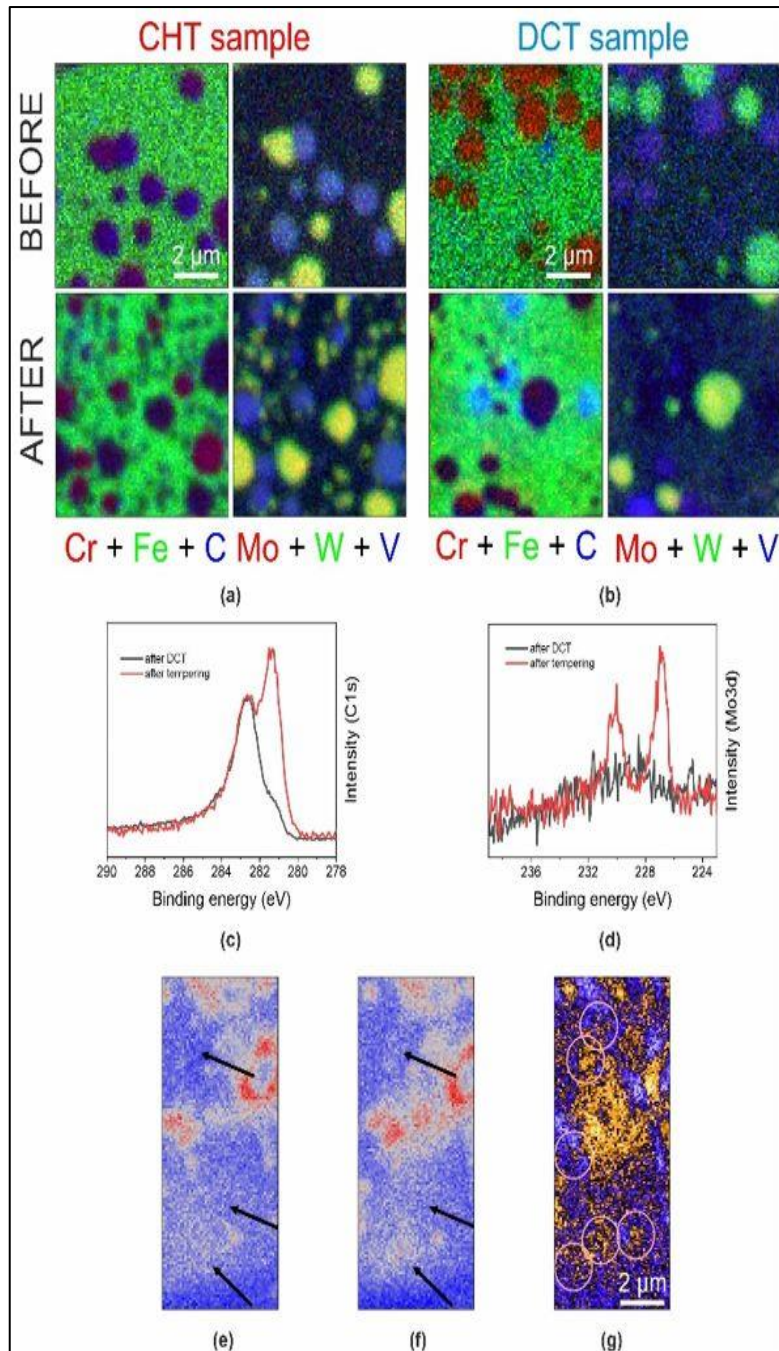
Fig. 3: SPEM color-coded maps of selected area for CHT (a) and DCT (b) samples before and after heating up to 873 K. XPS spectra (C 1s and Mo 3d) for MC carbide in DCT samples; after DCT and after heating up to 873 K (c)-(d). (e)-(g) in situ color-coded C 1s concentration maps of the DCT sample, e) before DCT, f) after DCT and tempering and g) after 24h in DCT. The pink circles in g) indicate changes in the C signal from the quenched state to the 24 h DCT cooled state.

before and after the DCT, we can confirm that the chemical shift changes are caused by the matrix, not by the carbides themselves. After heating up to 873 K, the shift returned to a binding state similar to that prior to DCT. This indicates a metastable transition state of Mo with DCT, which is relaxed by the application of thermal energy and the consequent precipitation and growth of carbides. Deconvolution of the metallic and oxide portions of the spectra reveals the non-uniform oxidation of the sample and reveals the newly formed Cr-enriched $M_{23}C_6$ carbides [37]. Furthermore, in-situ SPEM performed during DCT cooling showed that solely C develops

8

a change in spatial distribution during in-situ cooling (DCT) [24]. C segregation can be effectively visualised at micrometre resolution, which has not been reported before (Fig. 3(e)-(g)).

Exposure of HAFA to cryogenic temperatures results in C agglomeration in regions of around 100 nm. The observed changes in C and Mo spectra are associated with the evolution of loosely formed primordial M_2C carbides, which in the next step act as nucleation points for the next generations of carbides. Observation of Mo modification with DCT showed the enhanced formation of Mo-enriched M_7C_3 carbides. Newly modified M_7C_3 carbides are associated with a subtype of M_7C_3 that develops at cryogenic temperatures. In-situ SPEM observations also proved that the increased number of M_7C_3 carbides corresponds to increased nucleation and precipitation of $M_{23}C_6$ carbides with DCT.

3.3 In situ defect formation on MoS$_2$ thin films on Au foils by thermal annealing in hydrogen

Nowadays, there is a great interest to find sustainable materials for energy conversion. In this context, the research focused on cheap and abundant materials that could replace Pt in the hydrogen evolution reaction (HER) is gaining momentum. Some of the most promising materials are the transition metal chalcogenides (TMCs) i.e. sulphides, selenides and tellurides mainly of Mo and W or other transition metals (Ni, Co, etc). However, the main hurdle toward the technological implementation of TMDs is their poor activity, which is due to their modest electron conductivity and localization of the active sites limitedly at the edges. Therefore, it is mandatory to find ways for improving the catalytic performance of the TMDs by activation of the basal, through different strategies [38], such as the introduction of intrinsic or extrinsic defects i.e. vacancies, dopants, linear defects [39,40] or of secondary phases (graphene or layered double hydroxides). To unravel the role of chemical defects in TMDs we applied SPEM to investigate *in situ* monolayer films of MoS$_2$ with dendritic morphology during the thermal annealing in hydrogen, which is a well-known method to create sulphur vacancies.

The MoS$_2$ monolayer films were grown on polycrystalline Au metal foils using elemental S and MoO$_3$ sources according to the procedure outlined in Refs [41,42]. XPS confirms the presence of the 2H-MoS$_2$ polymorph whereas SEM was used to characterise the morphology of the films. The electron micrographs clearly indicate the formation of small triangular islands of about 3.5 µm in diameter and larger islands with irregular shape and lateral extension of about 100 µm (Fig. 4(a)). Notably the bigger islands are characterised by dendritic edges, which consist of narrow stripes a few µm wide, running parallel to each other for tenths of micrometres.
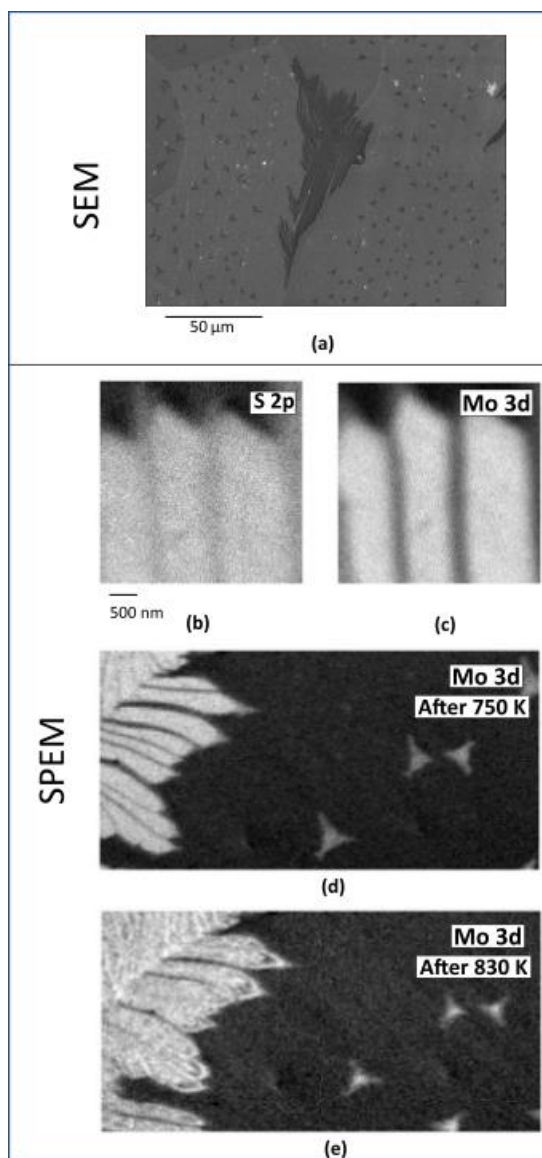
Fig. 4. (a)SEM images of MoS$_2$ films grown on Au foils, (b) and (c) SPEM Mo 3d and S 2p maps of the pristine sample, Mo 3d map after annealing at 750 K (d) and 830 K (e) in H$_2$.

Chemical maps of Mo 3d and S 2p were acquired before and during the dosing of H$_2$ (1 mbar) from room temperature up to 830 K (Fig. 4(b)-(e)). The Mo 3d spectrum of the pristine material can be described by a single Mo 3$d_{5/2}$ component at 229.4 eV BE, which is the typical value of stoichiometric 2H-MoS$_2$ [43]. The S 2p spectrum is more complex and, in addition to the component at 162.3 eV BE, distinctive of sulphides, entails two weaker peaks: at 161.3 eV, ascribed to elemental sulphur on the Au support, and at 163.6 eV BE, which can be associated with SO$_x$ species. During the annealing in H$_2$, the SPEM data clearly indicate that overall the morphology of the island remains the same and also the chemical composition does not change significantly up to 750 K (see Table 1 and Fig. 4(c) and (d)). Sets of Mo 3d and S 2p spectra, acquired at different temperatures, are shown in Fig. 5(a) and (b) respectively. The

chemical composition resulting from the analysis of the photoemission spectra at the different conditions are reported in Table 1.
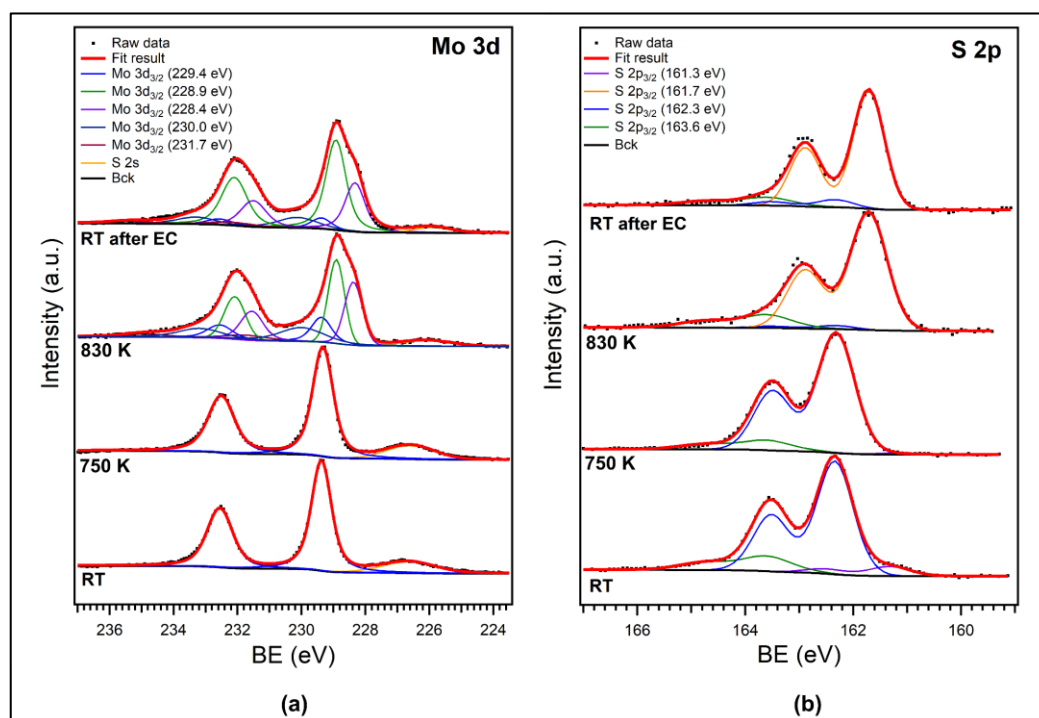

Fig. 5. High resolution core level (a) Mo 3d and (b) S 2p photoemission spectra of MoS$_2$ fractals at room temperature (RT), during annealing at 750 K and 830 K in H$_2$ 1 mbar atmosphere and after electrochemical measurements.

Table 1. Chemical composition of the islands at different temperatures

	Mo 3d [%]	S 2s [%]	S 2s/Mo 3d
RT after EC	66.2	33.8	0.51
830 K	64.6	35.4	0.55
750 K	34.5	65.5	1.90
710 K	34.6	65.4	1.89
670 K	35.3	64.7	1.83
RT	34.0	66.0	1.94

When a temperature of 830 K is reached, additional features appear in the Mo $3d$ spectrum and, in particular, two major components with the Mo $3d_{5/2}$ BE at 228.9 eV and 228.4 eV are becoming predominant. These new spectral features can be associated with different types of under coordinated Mo species, i.e. Mo ions next to S vacancies [44]. Indeed, several works suggest that as a consequence of thermal treatments in a reactive environment, the leaching of S species proceeds first with the elimination of S atoms from the basal plane with the formation of single point defects, however as the degree of defectivity increases, also clustered defects (line or vacancies islands) can be created [45,46]. The SPEM maps allow us to infer that first the reaction with H_2 starts at the edges of the islands especially on the small triangular ones, showing a clear corrosion and later expands also inward. However, as the reaction proceeds, some holes within the bigger dendrites become visible too, as indicated by the Mo $3d$ maps (Fig. 5(e)). This suggests that the S vacancies can eventually cluster forming vacancy islands, and conversely the Mo atoms should move in the opposite direction, leading to the formation of nanoscopic holes within the dendrites. On the other hand, there are no significant differences between the core level spectra, acquired on the bigger dendritic islands, compared to those of the smaller triangular islands.

The in situ H_2 dosing experiments on the MoS_2 thin films are therefore consistent with previous investigations on hydrothermally synthesised self-standing MoS_2 nanosheets, even though in that case the H_2 annealing temperature necessary to switch from the regime of single point defects to large region of Mo undercoordination was identified at 870 K.
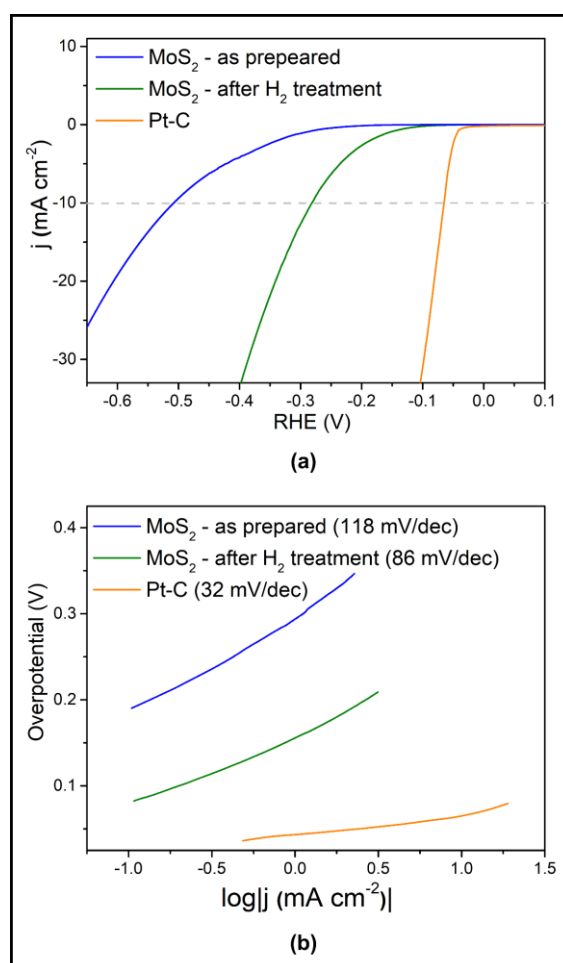

(a)

(b)

12

Fig. 3. Electrochemical activity of the hydrogen evolution reaction (HER) on metal dichalcogenide catalysts. (a) HER polarization curves, scan rate of 5 mV/s, 0.5 M H_2SO_4 as electrolyte, purged with Ar. (b) Tafel plot for the HER.

The MoS_2/Au thin films were tested towards the HER in acid condition before and after the H_2 treatment. The electrochemical (EC) HER measurements were carried out in a standard three-electrode electrochemical cell using an Autolab PGSTAT302 (Ecochemie) potentiostat. A carbon rod was used as a counter electrode, whereas a standard calomel electrode (SCE) electrode, calibrated with respect to the reversible hydrogen electrode (RHE), was the reference electrode. All potentials reported in the text and figures are referred to the (RHE) and corrected according to the equation: $E(RHE)=E(SCE) + 0.261$ V. The EC experiments were carried out in 0.5 M H_2SO_4 solution prepared from high-purity reagents (Sigma-Aldrich) and ultrapure Mill-Q water with a resistivity of 18.2 MΩ. As expected, the catalytic performance is significantly boosted by the introduction of a large number of S vacancies as shown in Fig. 3(a): in particular the overpotential to reach a current density of 10 mA/cm^2 decreases of about 220 mV passing from pristine, to H_2 treated samples, and also the Tafel slope varies from 118 mV/dec, a value widely reported for 2H-MoS_2, to 89 mV/dec (Fig. 3(b)).

Quite notably, the under stoichiometric phase of MoS_x formed after the H_2 treatment results to be very stable under electrochemical conditions, and in particular the Mo 3d spectra prior and after the electrochemical tests are identical. This demonstrates that even though we are dealing with a monolayer system with highly under coordinated Mo atoms, there is no significant tendency of the metal centres to regain their initial coordination by binding to water or oxo/hydroxo species, readily available in the electrochemical environment.

3.4   Near ambient pressure: highlighting the dynamics of graphene protection toward the oxidation of copper under operando conditions

Graphene has been very extensively studied and there are precise XPS fingerprints of suspended single layers as shown in section 3.1 [22], doping and functionalization [47–50], and device properties [51,52], to name a few of them. In all these experiments, the possibility to characterise the graphene at the individual flake level, to distinguish single layers from multi-layers and to see lateral interfaces with other materials, are the among greatest advantages of spectro-microscopy techniques. Many peculiar properties of this 2D material also require to study of its interactions with gases at near-ambient conditions that has become already possible with classic ambient pressure XPS. Graphene, indeed, is a good playground to follow the kinetics of undercover catalysis where reactions can take place at the interface of graphene and catalyst substrate [53]. Metal-free heteroatom doped-graphene is itself catalytically active for many reactions: oxygen reduction reaction (ORR) [54,55], NO decomposition [56], among others. Another important property of graphene is its no permeability which makes it an optimum candidate as an anticorrosive coating for metal surfaces exposed to aggressive environments, such as high pressure of oxidising gases at high temperatures, which are conditions typical for materials used in car engines, as an example. Even though a graphene flake within the grain is impermeable, some intercalation of gas molecules may occur at the boundaries or defect sites and may interact with the

underlying substrate. The possibility to study these phenomena with spatial resolution and in realistic conditions is, therefore, of fundamental importance.

Operando near-ambient-pressure photoemission spectromicroscopy measurements of graphene-coated copper heated in oxygen atmosphere (623 K, up to 0.1 mbar) were performed using the constructed SPEM near ambient pressure cell (NAP-cell). The cell encapsulates the sample within a closed volume and keeps the high-pressure environment locally confined. A technical description of this setup can be found in Refs [57–59]. Regions with bare Cu and areas covered with mono- and bi-layer graphene flakes were investigated.
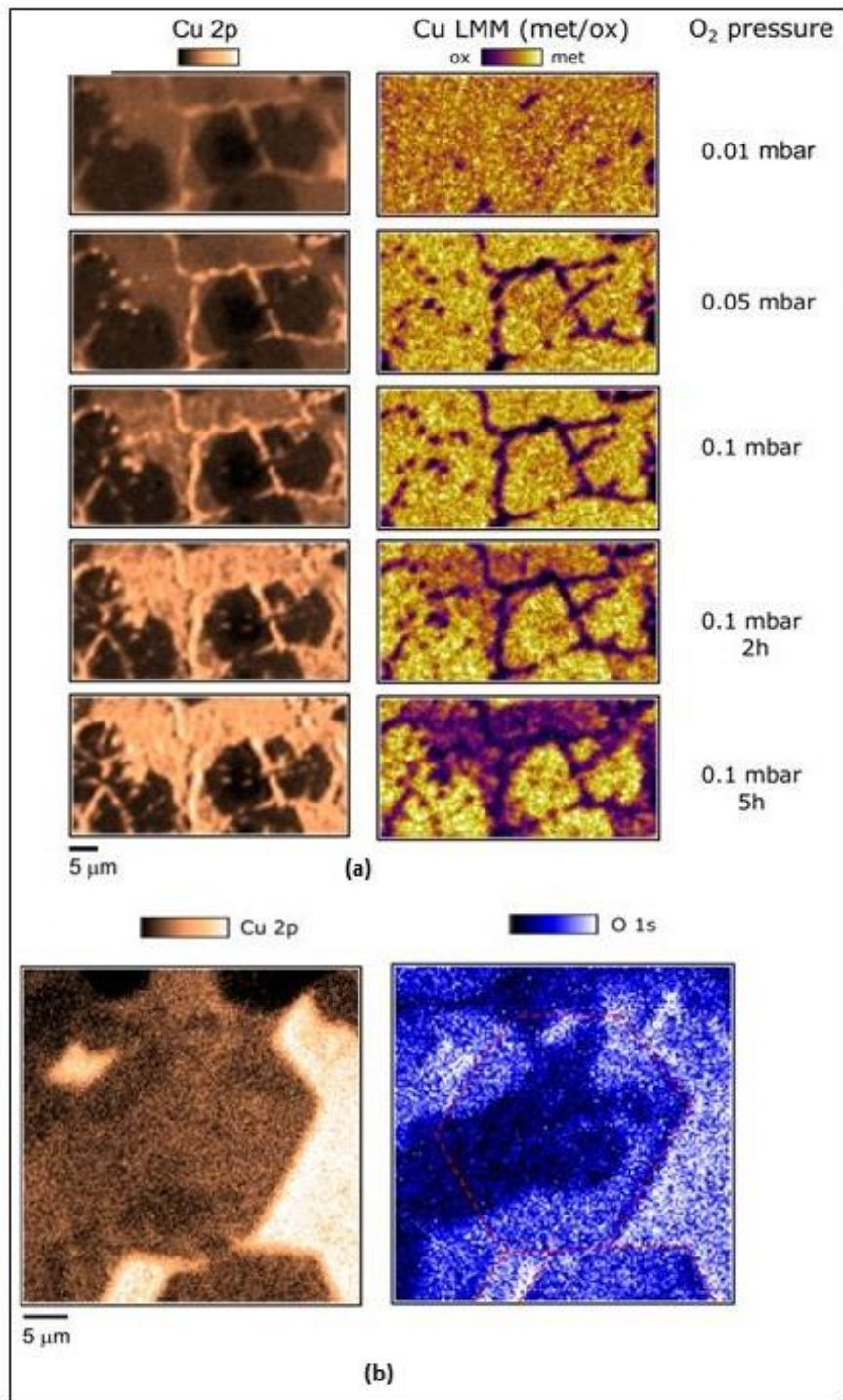
Fig. 6. (a) Cu 2p (left) and Cu LMM (right) photoemission maps at different oxygen pressures and constant temperature (623 K). b) Cu 2p (left) and O 1s (right) photoemission maps at 0.1 mbar O_2 and 623 K. The red dotted lines indicate individual graphene flakes.

Figure 6(a) shows two series of maps obtained by recording the photoelectrons emitted from the Cu 2p core level (left) and from Cu LMM Auger (right) at constant temperature (623 K) and increasing oxygen pressure (from 0.01 to 0.1 mbar). In the copper map, the dark areas are the graphene flakes: grey is the single layer and black is the bilayer. Upon exposure to

increasing pressure of oxygen, the Cu $2p$ images appear brighter (higher copper signal) showing a disappearance of the C coverage starting from the grain boundaries. In the last image, after 5 hours of exposure to 0.1 mbar of O_2, traces of carbon removal are also visible inside some graphene flakes. The Cu Auger signal is a good fingerprint to easily distinguish the oxidation state of copper because the main LMM lines of Cu(0) and Cu(I) are separated by approximately 2 eV [60]. The ratio of the two maps acquired at the Cu(0) and Cu(I) energies is shown in Fig. 6(a)-right columns: the darker regions indicate the presence of Cu_2O, while brighter regions correspond to metallic Cu. From both series of maps, it can be seen that bare copper regions progressively extend, at the expense of graphene, which is etched away, and the exposed metallic surface is oxidised, while the copper protected by graphene remains metallic. In these maps, several bilayer flakes are evident: those regions are still present after 5 hours of exposure, even if with evident signs of pitch defects where oxygen intercalates and locally oxidises the copper.

Fig.6(b) shows two Cu $2p$ (left) and O $1s$ (right) magnified maps of the surface after O_2 exposure at high T; hexagonal graphene flakes of about 15 µm in lateral dimension can be easily identified from the image contrast, which is proportional to the intensity of the respective core level. In the Cu map, the brightest regions correspond to bare Cu, darkest to graphene. In the oxygen map, one hexagonal flake is highlighted by red dotted lines. It can be noted that the colour contrast in the Cu $2p$ map varies within the same hexagonal flake: it is brighter towards the centre, indicating a less intense copper signal at the edges of the flake. On the contrary, the O $1s$ map shows an opposite behaviour: the O $1s$ signal is higher on the bare copper region, indicating an oxidation of the substrate at these conditions, and then is darker at the centre of the flake. This is an indication of oxygen intercalation at the edges of the graphene flake, which therefore slightly suppresses the intensity of Cu $2p$, and, as demonstrated in Fig. 6(a), it is responsible for copper oxidation.

Similar experiments by using NO_2 instead of O_2, resulting in a higher and faster aggressiveness of the oxidation, have also been performed [61]; in that case the formation of Cu(II) was observed as well. Reports on hexagonal boron nitride (hBN), another 2D material structurally similar to graphene, but insulator, show a different behaviour to graphene: the oxidation of copper doesn't spread in the same way due to the absence of galvanic corrosion, hBN being an insulator. In the long term, the performance of hBN as a corrosion inhibitor appears to be higher [62–64].

The key in this study was the combination of spatial and chemical resolution of the SPEM operating in a near-ambient-pressure environment, thus allowing us to overcome both the material and pressure gap and to observe in real-time with high spatial resolution the protection mechanism of graphene to copper oxidation. The ability to perform spatially resolved XPS and imaging at high pressures has allowed for the first time a unique characterization of the oxidation phenomena pushing the limits of this technique from fundamental studies to realistic material exploration under working conditions. Although bare Cu oxidises naturally at room temperature, our results demonstrate that a graphene coating acts as an effective barrier to prevent copper oxidation even at high temperatures with oxygen intercalation beneath graphene starting from boundaries and defects is slow. We also show that bilayer flakes can protect at even higher temperatures. The protected metallic substrate, therefore, does not suffer corrosion, preserving its metallic character, and making this coating

appealing for any application in an aggressive atmospheric environment and high temperatures.

Conclusions

The most recent technical developments of the SPEM hosted at the ESCA Microscopy beamline at the Elettra synchrotron light facility are addressed by using the results of recently performed four standard and unconventional experiments. In the first study the analysis of suspended graphene layers has complemented electron microscopy and Raman spectroscopy results. Current technology allows the production of 2D materials in the form of very small flakes when a controlled thickness in the monolayer range is needed; moreover within the same flake the defects and/or contamination free areas are not larger than a few tens of nm. Guided by the TEM images the SPEM was capable of identifying and studying such regions. In the second experiment a cryogenic setup, used to investigate the effect of DCT on a HAFA, where sample temperatures as low as 123 K, allowed to analyze by imaging and microspectroscopy the carbide evolution and chemical shifts of alloying elements. The third example revealed the capability of SPEM to perform *operando* measurements at high temperature and gas pressure without affecting the spatial resolution of the microscope. Chemical evolution of MoS_2 thin flakes, a promising material for HER platinum free devices, is analysed at different annealing temperatures and H_2 pressure and SPEM with high spatial resolution identifies the generation of under coordinated Mo atoms. In the last example the NAP-Cell developed at ESCA Microscopy has allowed SPEM measurements at pressures as high as 1 mbar and sample temperatures up to 900 K to investigate graphene-coated copper foils under oxidizing conditions. The study demonstrated that graphene cover hinders the oxidation of copper in an aggressive environment and at high temperatures, whereas bare copper oxidizes already naturally even at room temperature. These results show the great potential of graphene as a stable protective layer for retarding the formation of metal oxides, since the oxygen penetration even with single layer graphene can occur only through the defect sites. Along with further efforts for pushing the lateral resolution that should be done by having more efficient spectrometers, since the radiation damage with increasing the photon flux in the microspot is serious issue, the recent considerable achievements in sample environment to break the pressure gap and characterize materials in their operando conditions is extremely important. These means not only gases at ambient pressure but also operating conditions with applied external magnetic, electric and light fields towards a full integration of methodologies for *operando* analysis.

.

References

[1]   H. Ade, J. Kirz, S.L. Hulbert, E.D. Johnson, E. Anderson, D. Kern, X-ray spectromicroscopy with a zone plate generated microprobe, Appl Phys Lett. 56 (1990) 1841–1843. https://doi.org/10.1063/1.103064.

[2]   E. Bauer, A brief history of PEEM, J Electron Spectros Relat Phenomena. 185 (2012) 314–322. https://doi.org/10.1016/j.elspec.2012.08.001.

[3]   M. Amati, A. Barinov, V. Feyer, L. Gregoratti, M. Al-Hada, A. Locatelli, T.O. Mentes, H. Sezen, C.M. Schneider, M. Kiskinova, Photoelectron microscopy at Elettra: Recent advances and perspectives, J Electron Spectros Relat Phenomena. 224 (2018) 59–67. https://doi.org/10.1016/j.elspec.2017.06.006.

[4]   M. Amati, A. Barinov, L. Gregoratti, H. Sezen, M. Kiskinova, Scanning Photoelectron Microscopy: Past, Present and Future, in: 2020: pp. 427–448. https://doi.org/10.1007/978-3-030-46906-1_14.

[5]   J.-W. Chen, S.-T. Lo, S.-C. Ho, S.-S. Wong, T.-H.-Y. Vu, X.-Q. Zhang, Y.-D. Liu, Y.-Y. Chiou, Y.-X. Chen, J.-C. Yang, Y.-C. Chen, Y.-H. Chu, Y.-H. Lee, C.-J. Chung, T.-M. Chen, C.-H. Chen, C.-L. Wu, A gate-free monolayer WSe2 pn diode, Nat Commun. 9 (2018) 3143. https://doi.org/10.1038/s41467-018-05326-x.

[6]   K. Akada, T. Sudayama, D. Asakura, H. Kitaura, N. Nagamura, K. Horiba, M. Oshima, E. Hosono, Y. Harada, Microscopic photoelectron analysis of single crystalline LiCoO2 particles during the charge-discharge in an all solid-state lithium ion battery, Sci Rep. 9 (2019). https://doi.org/10.1038/s41598-019-48842-6.

[7]   K. Schweinar, R.L. Nicholls, C.R. Rajamathi, P. Zeller, M. Amati, L. Gregoratti, D. Raabe, M. Greiner, B. Gault, O. Kasian, Probing catalytic surfaces by correlative scanning photoemission electron microscopy and atom probe tomography, J Mater Chem A Mater. 8 (2020) 388–400. https://doi.org/10.1039/C9TA10818A.

[8]   B. Rösner, P. Dudin, J. Bosgra, M. Hoesch, C. David, Zone plates for angle-resolved photoelectron spectroscopy providing sub-micrometre resolution in the extreme ultraviolet regime, J Synchrotron Radiat. 26 (2019) 467–472. https://doi.org/10.1107/S1600577519000869.

[9]   J. Avila, I. Razado-Colambo, S. Lorcy, B. Lagarde, J.-L. Giorgetta, F. Polack, M.C. Asensio, ANTARES, a scanning photoemission microscopy beamline at SOLEIL, J Phys Conf Ser. 425 (2013) 192023. https://doi.org/10.1088/1742-6596/425/19/192023.

[10]   P. Dudin, P. Lacovig, C. Fava, E. Nicolini, A. Bianco, G. Cautero, A. Barinov, Angle-resolved photoemission spectroscopy and imaging with a submicrometre probe at the SPECTROMICROSCOPY-3.2L beamline of Elettra, J Synchrotron Radiat. 17 (2010) 445–450. https://doi.org/10.1107/S0909049510013993.

[11]   G. Kim, Y. Yu, H. Lim, B. Jeong, J. Lee, J. Baik, B.S. Mun, K. Kim, AP-XPS beamline, a platform for operando science at Pohang Accelerator Laboratory, J Synchrotron Radiat. 27 (2020) 507–514. https://doi.org/10.1107/S160057751901676X.

[12]   K. Horiba, Y. Nakamura, N. Nagamura, S. Toyoda, H. Kumigashira, M. Oshima, K. Amemiya, Y. Senba, H. Ohashi, Scanning photoelectron microscope for nanoscale three-dimensional spatial-resolved electron spectroscopy for chemical analysis, Review of Scientific Instruments. 82 (2011) 113701. https://doi.org/10.1063/1.3657156.

[13]   M. Marsi, L. Casalis, L. Gregoratti, S. Günther, A. Kolmakov, J. Kovac, D. Lonza, M. Kiskinova, ESCA Microscopy at ELETTRA: what it is like to perform spectromicroscopy experiments on a third generation synchrotron radiation source, J Electron Spectros Relat Phenomena. 84 (1997) 73–83. https://doi.org/10.1016/S0368-2048(97)00010-8.

[14]   https://www.elettra.eu/elettra-beamlines/escamicroscopy.html, (n.d.).

[15] L. Gregoratti, A. Barinov, E. Benfatto, G. Cautero, C. Fava, P. Lacovig, D. Lonza, M. Kiskinova, R. Tommasini, S. Mähl, W. Heichler, 48-Channel electron detector for photoemission spectroscopy and microscopy, Review of Scientific Instruments. 75 (2004) 64–68. https://doi.org/10.1063/1.1630837.

[16] S. Doniach, M. Sunjic, Many-electron singularity in X-ray photoemission and X-ray line spectra from metals, Journal of Physics C: Solid State Physics. 3 (1970) 285–291. https://doi.org/10.1088/0022-3719/3/2/010.

[17] S. Lizzit, G. Zampieri, L. Petaccia, R. Larciprete, P. Lacovig, E.D.L. Rienks, G. Bihlmayer, A. Baraldi, P. Hofmann, Band dispersion in the deep 1s core level of graphene, Nat Phys. 6 (2010) 345–349. https://doi.org/10.1038/nphys1615.

[18] K.C. Prince, I. Ulrych, M. Peloi, B. Ressel, V. Cháb, C. Crotti, C. Comicioli, Core-level photoemission from graphite, Phys Rev B. 62 (2000) 6866–6868. https://doi.org/10.1103/PhysRevB.62.6866.

[19] A.B. Preobrajenski, M.L. Ng, A.S. Vinogradov, N. Mårtensson, Controlling graphene corrugation on lattice-mismatched substrates, Phys Rev B. 78 (2008) 073401. https://doi.org/10.1103/PhysRevB.78.073401.

[20] A. Grüneis, K. Kummer, D. V Vyalikh, Dynamics of graphene growth on a metal surface: a time-dependent photoemission study, New J Phys. 11 (2009) 073050. https://doi.org/10.1088/1367-2630/11/7/073050.

[21] H. Hibino, H. Kageshima, M. Nagase, Epitaxial few-layer graphene: towards single crystal growth, J Phys D Appl Phys. 43 (2010) 374005. https://doi.org/10.1088/0022-3727/43/37/374005.

[22] T. Susi, M. Scardamaglia, K. Mustonen, M. Tripathi, A. Mittelberger, M. Al-Hada, M. Amati, H. Sezen, P. Zeller, A.H. Larsen, C. Mangler, J.C. Meyer, L. Gregoratti, C. Bittencourt, J. Kotakoski, Intrinsic core level photoemission of suspended monolayer graphene, Phys Rev Mater. 2 (2018) 074005. https://doi.org/10.1103/PhysRevMaterials.2.074005.

[23] P. Jovičević-Klug, B. Podgornik, Review on the Effect of Deep Cryogenic Treatment of Metallic Materials in Automotive Applications, Metals (Basel). 10 (2020) 434. https://doi.org/10.3390/met10040434.

[24] P. Jovičević-Klug, L. Tegg, M. Jovičević-Klug, R. Parmar, M. Amati, L. Gregoratti, L. Almásy, J.M. Cairney, B. Podgornik, Understanding carbide evolution and surface chemistry during deep cryogenic treatment in high-alloyed ferrous alloy, Appl Surf Sci. 610 (2023) 155497. https://doi.org/10.1016/j.apsusc.2022.155497.

[25] P. Jovičević-Klug, M. Jovičević-Klug, L. Tegg, D. Seidler, L. Thormählen, R. Parmar, M. Amati, L. Gregoratti, J.M. Cairney, J. McCord, M. Rohwerder, B. Podgornik, Correlative surface and bulk analysis of deep cryogenic treatment influence on high-alloyed ferrous alloy, Journal of Materials Research and Technology. 21 (2022) 4799–4810. https://doi.org/10.1016/j.jmrt.2022.11.075.

[26] P. Jovičević-Klug, A.Z. Guštin, M. Jovičević-Klug, B. Šetina Batič, A. Lebar, B. Podgornik, Coupled role of alloying and manufacturing on deep cryogenic treatment performance on high-alloyed ferrous alloys, Journal of Materials Research and Technology. 18 (2022) 3184–3197. https://doi.org/10.1016/j.jmrt.2022.04.025.

[27]   P. Baldissera, C. Delprete, Deep Cryogenic Treatment: A Bibliographic Review, The Open Mechanical Engineering Journal. 2 (2008) 1–11. https://doi.org/10.2174/1874155X00802010001.

[28]   P. balajiT, REVIEW ON CRYOGENIC TREARMENT OF STEELS, International Research Journal of Engineering and Technology. (2016). www.irjet.net.

[29]   T. Sonar, S. Lomte, C. Gogte, Cryogenic Treatment of Metal – A Review, Mater Today Proc. 5 (2018) 25219–25228. https://doi.org/10.1016/j.matpr.2018.10.324.

[30]   N.S. Kalsi, R. Sehgal, V.S. Sharma, Cryogenic Treatment of Tool Materials: A Review, Materials and Manufacturing Processes. 25 (2010) 1077–1100. https://doi.org/10.1080/10426911003720862.

[31]   M. Jovičević-Klug, P. Jovičević-Klug, J. McCord, B. Podgornik, Investigation of microstructural attributes of steel surfaces through magneto-optical Kerr effect, Journal of Materials Research and Technology. 11 (2021) 1245–1259. https://doi.org/10.1016/j.jmrt.2021.01.106.

[32]   E. Demir, ˙I Tokta¸stokta¸s, Effects of cryogenic treatment on residual stresses of AISI D2 tool steel, 56 (2018) 153–161. https://doi.org/10.4149/km.

[33]   P. Jovičević-Klug, M. Jovičević-Klug, B. Podgornik, Unravelling the Role of Nitrogen in Surface Chemistry and Oxidation Evolution of Deep Cryogenic Treated High-Alloyed Ferrous Alloy, Coatings. 12 (2022) 213. https://doi.org/10.3390/coatings12020213.

[34]   P. Jovičević-Klug, M. Sedlaček, M. Jovičević-Klug, B. Podgornik, Effect of Deep Cryogenic Treatment on Wear and Galling Properties of High-Speed Steels, Materials. 14 (2021) 7561. https://doi.org/10.3390/ma14247561.

[35]   P. Jovičević-Klug, M. Jovičević-Klug, B. Podgornik, Effectiveness of deep cryogenic treatment on carbide precipitation, Journal of Materials Research and Technology. 9 (2020) 13014–13026. https://doi.org/10.1016/j.jmrt.2020.09.063.

[36]   D.V. Suetin, I.R. Shein, A.L. Ivanovskii, Structural, electronic and magnetic properties of η carbides (Fe_3W_3C, Fe_6W_6C, Co_3W_3C and Co_6W_6C) from first principles calculations, Physica B Condens Matter. 404 (2009) 3544–3549. https://doi.org/10.1016/j.physb.2009.05.051.

[37]   L. Gregoratti, A. Barinov, E. Benfatto, G. Cautero, C. Fava, P. Lacovig, D. Lonza, M. Kiskinova, R. Tommasini, S. Mähl, W. Heichler, 48-Channel electron detector for photoemission spectroscopy and microscopy, Review of Scientific Instruments. 75 (2004) 64–68. https://doi.org/10.1063/1.1630837.

[38]   X. Wu, H. Zhang, J. Zhang, X.W. (David) Lou, Recent Advances on Transition Metal Dichalcogenides for Electrochemical Energy Conversion, Advanced Materials. 33 (2021) 2008376. https://doi.org/10.1002/adma.202008376.

[39]   M. Lunardon, M. Cattelan, S. Agnoli, G. Granozzi, Toward sustainable and effective HER electrocatalysts: Strategies for the basal plane site activation of transition metal dichalcogenides, Curr Opin Electrochem. 34 (2022) 101025. https://doi.org/10.1016/j.coelec.2022.101025.

[40]   M. Lunardon, T. Kosmala, M. Ghorbani-Asl, A. V. Krasheninnikov, S. Kolekar, C. Durante, M. Batzill, S. Agnoli, G. Granozzi, Catalytic Activity of Defect-Engineered Transition Me tal Dichalcogenides Mapped with Atomic-Scale Precision by Electrochemical Scanning Tunneling

Microscopy, ACS Energy Lett. 8 (2023) 972–980.
https://doi.org/10.1021/acsenergylett.2c02599.

[41]   Y. Zhang, Q. Ji, J. Wen, J. Li, C. Li, J. Shi, X. Zhou, K. Shi, H. Chen, Y. Li, S. Deng, N. Xu, Z. Liu, Y. Zhang, Monolayer MoS$_2$ Dendrites on a Symmetry-Disparate SrTiO$_3$ (001) Substrate: Formation Mechanism and Interface Interaction, Adv Funct Mater. 26 (2016) 3299–3305. https://doi.org/10.1002/adfm.201505571.

[42]   J. Hu, W. Quan, P. Yang, F. Cui, F. Liu, L. Zhu, S. Pan, Y. Huan, F. Zhou, J. Fu, G. Zhang, P. Gao, Y. Zhang, Epitaxial Growth of High-Quality Monolayer MoS$_2$ Single Crystals on Low-Symmetry Vicinal Au(101) Facets with Different Miller Indices, ACS Nano. 17 (2023) 312–321. https://doi.org/10.1021/acsnano.2c07978.

[43]   F. Carraro, L. Calvillo, M. Cattelan, M. Favaro, M. Righetto, S. Nappini, I. Píš, V. Celorrio, D.J. Fermín, A. Martucci, S. Agnoli, G. Granozzi, Fast One-Pot Synthesis of MoS$_2$/Crumpled Graphene p–n Nanonjunctions for Enhanced Photoelectrochemical Hydrogen Production, ACS Appl Mater Interfaces. 7 (2015) 25685–25692. https://doi.org/10.1021/acsami.5b06668.

[44]   F. Bussolotti, J. Chai, M. Yang, H. Kawai, Z. Zhang, S. Wang, S.L. Wong, C. Manzano, Y. Huang, D. Chi, K.E.J. Goh, Electronic properties of atomically thin MoS$_2$ layers grown by physical vapour deposition: band structure and energy level alignment at layer/substrate interfaces, RSC Adv. 8 (2018) 7744–7752. https://doi.org/10.1039/C8RA00635K.

[45]   L. Li, Z. Qin, L. Ries, S. Hong, T. Michel, J. Yang, C. Salameh, M. Bechelany, P. Miele, D. Kaplan, M. Chhowalla, D. Voiry, Role of Sulfur Vacancies and Undercoordinated Mo Regions in MoS$_2$ Nanosheets toward the Evolution of Hydrogen, ACS Nano. 13 (2019) 6824–6834. https://doi.org/10.1021/acsnano.9b01583.

[46]   M. Liu, J. Shi, Y. Li, X. Zhou, D. Ma, Y. Qi, Y. Zhang, Z. Liu, Temperature-Triggered Sulfur Vacancy Evolution in Monolayer MoS$_2$/Graphene Heterostructures, Small. 13 (2017) 1602967. https://doi.org/10.1002/smll.201602967.

[47]   C. Struzzi, M. Scardamaglia, N. Reckinger, J.-F. Colomer, H. Sezen, M. Amati, L. Gregoratti, R. Snyders, C. Bittencourt, Fluorination of suspended graphene, Nano Res. 10 (2017) 3151–3163. https://doi.org/10.1007/s12274-017-1532-4.

[48]   C. Struzzi, H. Sezen, M. Amati, L. Gregoratti, N. Reckinger, J.-F. Colomer, R. Snyders, C. Bittencourt, M. Scardamaglia, Fluorine and sulfur simultaneously co-doped suspended graphene, Appl Surf Sci. 422 (2017) 104–110. https://doi.org/10.1016/j.apsusc.2017.05.258.

[49]   C. Struzzi, M. Scardamaglia, N. Reckinger, H. Sezen, M. Amati, L. Gregoratti, J.-F. Colomer, C. Ewels, R. Snyders, C. Bittencourt, Probing plasma fluorinated graphene *via* spectromicroscopy, Physical Chemistry Chemical Physics. 19 (2017) 31418–31428. https://doi.org/10.1039/C7CP05305C.

[50]   M. Scardamaglia, B. Aleman, M. Amati, C. Ewels, P. Pochet, N. Reckinger, J.-F. Colomer, T. Skaltsas, N. Tagmatarchis, R. Snyders, L. Gregoratti, C. Bittencourt, Nitrogen implantation of suspended graphene flakes: Annealing effects and selectivity of sp2 nitrogen species, Carbon N Y. 73 (2014) 371–381. https://doi.org/10.1016/j.carbon.2014.02.078.

[51]   J. Aprojanz, Ph. Rosenzweig, T.T.N. Nguyen, H. Karakachian, K. Küster, U. Starke, M. Lukosius, G. Lippert, A. Sinterhauf, M. Wenderoth, A.A. Zakharov, C. Tegenkamp, High-Mobility

Epitaxial Graphene on Ge/Si(100) Substrates, ACS Appl Mater Interfaces. 12 (2020) 43065–43072. https://doi.org/10.1021/acsami.0c10725.

[52] H. Li, Y. Shi, H. Shang, W. Wang, J. Lu, A.A. Zakharov, L. Hultman, R.I.G. Uhrberg, M. Syväjärvi, R. Yakimova, L. Zhang, J. Sun, Atomic-Scale Tuning of Graphene/Cubic SiC Schottky Junction for Stable Low-Bias Photoelectrochemical Solar-to-Fuel Conversion, ACS Nano. 14 (2020) 4905–4915. https://doi.org/10.1021/acsnano.0c00986.

[53] V. Boix, M. Scardamaglia, T. Gallo, G. D'Acunto, M.D. Strømsheim, F. Cavalca, S. Zhu, A. Shavorskiy, J. Schnadt, J. Knudsen, Following the Kinetics of Undercover Catalysis with APXPS and the Role of Hydrogen as an Intercalation Promoter, ACS Catal. 12 (2022) 9897–9907. https://doi.org/10.1021/acscatal.2c00803.

[54] L. Qu, Y. Liu, J.-B. Baek, L. Dai, Nitrogen-Doped Graphene as Efficient Metal-Free Electrocatalyst for Oxygen Reduction in Fuel Cells, ACS Nano. 4 (2010) 1321–1326. https://doi.org/10.1021/nn901850u.

[55] M. Scardamaglia, T. Susi, C. Struzzi, R. Snyders, G. Di Santo, L. Petaccia, C. Bittencourt, Spectroscopic observation of oxygen dissociation on nitrogen-doped graphene, Sci Rep. 7 (2017) 7960. https://doi.org/10.1038/s41598-017-08651-1.

[56] Y. Wang, Y. Shen, Y. Zhou, Z. Xue, Z. Xi, S. Zhu, Heteroatom-Doped Graphene for Efficient NO Decomposition by Metal-Free Catalysis, ACS Appl Mater Interfaces. 10 (2018) 36202–36210. https://doi.org/10.1021/acsami.8b09503.

[57] H. Sezen, M. Al-Hada, M. Amati, L. Gregoratti, *In situ* chemical and morphological characterization of copper under near ambient reduction and oxidation conditions, Surface and Interface Analysis. 50 (2018) 921–926. https://doi.org/10.1002/sia.6276.

[58] B. Bozzini, D. Kuscer, S. Drnovšek, M. Al-Hada, M. Amati, H. Sezen, L. Gregoratti, Spatially Resolved Photoemission and Electrochemical Characterization of a Single-Chamber Solid Oxide Fuel Cell, Top Catal. 61 (2018) 2185–2194. https://doi.org/10.1007/s11244-018-1064-5.

[59] L. Gregoratti, M. Al-Hada, M. Amati, R. Brescia, D. Roccella, H. Sezen, P. Zeller, Spatially Resolved Photoelectron Spectroscopy from Ultra-high Vacuum to Near Ambient Pressure Sample Environments, Top Catal. 61 (2018) 1274–1282. https://doi.org/10.1007/s11244-018-0982-6.

[60] M. Scardamaglia, C. Struzzi, A. Zakharov, N. Reckinger, P. Zeller, M. Amati, L. Gregoratti, Highlighting the Dynamics of Graphene Protection toward the Oxidation of Copper Under Operando Conditions, ACS Appl Mater Interfaces. 11 (2019) 29448–29457. https://doi.org/10.1021/acsami.9b08918.

[61] M. Amati, L. Gregoratti, P. Zeller, M. Greiner, M. Scardamaglia, B. Junker, T. Ruß, U. Weimar, N. Barsan, M. Favaro, A. Alharbi, I.J.T. Jensen, A. Ali, B.D. Belle, Near ambient pressure photoelectron spectro-microscopy: from gas–solid interface to operando devices, J Phys D Appl Phys. 54 (2021) 204004. https://doi.org/10.1088/1361-6463/abe5e2.

[62] M. Scardamaglia, V. Boix, G. D'Acunto, C. Struzzi, N. Reckinger, X. Chen, A. Shivayogimath, T. Booth, J. Knudsen, Comparative study of copper oxidation protection with graphene and hexagonal boron nitride, Carbon N Y. 171 (2021) 610–617. https://doi.org/10.1016/j.carbon.2020.09.021.

[63]   L. Shen, Y. Zhao, Y. Wang, R. Song, Q. Yao, S. Chen, Y. Chai, A long-term corrosion barrier with
        an insulating boron nitride monolayer, J Mater Chem A Mater. 4 (2016) 5044–5050.
        https://doi.org/10.1039/C6TA01604A.

[64]   M. Galbiati, A.C. Stoot, D.M.A. Mackenzie, P. Bøggild, L. Camilli, Real-time oxide evolution of
        copper protected by graphene and boron nitride barriers, Sci Rep. 7 (2017) 39770.
        https://doi.org/10.1038/srep39770.